PCCP

ROYAL SOCIETY OF CHEMISTRY

PAPER

View Article Online
View Journal | View Issue

Cite this: *Phys. Chem. Chem. Phys.*, 2025, **27**, 2817

Sensing of *n*-butanol vapours using an oxygen vacancy-enriched Zn_2SnO_4–SnO_2 hybrid-composite†

Reshmi Thekke Parayil,‡[ab] Snehangshu Paine,‡[c] K. Mukherjee,*[c] D. Tyagi,[d] Manoj Mohapatra[ab] and Santosh K. Gupta*[ab]

Received 23rd October 2024,
Accepted 30th December 2024

DOI: 10.1039/d4cp04070h

rsc.li/pccp

The precise identification of various toxic gases is important to prevent health and environmental hazards using cost-effective, efficient, metal oxide-based chemiresistive sensing methods. This study explores the sensing properties of a chemiresistive sensor based on a Zn_2SnO_4–SnO_2 microcomposite for detecting *n*-butanol vapours. The microcomposite, enriched with oxygen vacancies, was thoroughly characterized, confirming its structure, crystallinity, morphology and elemental composition. The sensor demonstrated high repeatability across a temperature range of 275–350 °C and concentrations from 100 to 1000 ppm, with the highest response observed at 350 °C. The concentration-dependent response of the sensor towards *n*-butanol follows a linear relationship within the studied operating temperature range. The response time increases as the concentration of *n*-butanol increases. Conductance transients were modelled using the Langmuir–Hinshelwood mechanism, showing temperature-dependent oxidation kinetics. At lower temperatures, the rate-determining step involved *n*-butanol oxidation, while at higher temperatures, simultaneous oxidation and desorption processes dominated. The calculated activation energy for the *n*-butanol oxidation step was 0.12 eV. Furthermore, principal component analysis (PCA) effectively discriminated *n*-butanol from other volatile organic compounds (VOCs), emphasizing the sensor's potential for selective *n*-butanol detection through a combination of kinetic modelling and statistical analysis.

1. Introduction

Recently, gas sensors based on semiconductor metal oxides (SMOs) have attracted attention owing to their simple analysis techniques for sensing volatile organic compounds. Considering their excellent sensitivity, rapid response-recovery time, and concise preparation process, metal oxide semiconductors such as SnO_2, WO_3, ZnO, NiO, and In_2O_3 have been used as gas sensing materials.[1,2]

Zn_2SnO_4 is a ternary n-type semiconductor oxide with a wide band gap of 3.6 eV that finds applications in photocatalysis, solar cells and gas sensing.[1,3] This ternary oxide has been explored for sensing many volatile organic compounds such as butanol, ethanol, acetone, formaldehyde and toluene.[4] In fact, our group has demonstrated excellent gas sensing properties of pristine Zn_2SnO_4 enriched with oxygen vacancies towards *n*-butanol.[5] Defects have played a profound role in dictating the performance of oxide-based compounds towards gas sensing.[6–8] SnO_2 is a wide band gap n-type semiconductor that has been known for its promising gas sensing performance and can create heterostructure with other metal oxides, leading to an enhancement in its gas sensing response.[9]

Both Zn_2SnO_4 and SnO_2 are good choices for gas sensing applications, and the combination of the two is expected to have enhanced gas-sensing properties. It was observed that coupling two metal oxides possessing different band gap values improves the physical and chemical properties by affecting electron–hole pairs.[10] Here, the conduction band edge of Zn_2SnO_4 is more negative than the conduction band edge of SnO_2. Therefore, electrons will transfer from Zn_2SnO_4 to SnO_2 until Fermi level alignment is reached, which results in enhancement of electron–hole pair separation and free electron density.

There are plenty of reports in which researchers have delved into the gas-sensing properties of ZnO, SnO_2 and Zn_2SnO_4

[a] *Radiochemistry Division, Bhabha Atomic Research Centre, Trombay, Mumbai-400085, India. E-mail: santoshg@barc.gov.in*
[b] *Homi Bhabha National Institute, Anushaktinagar, Mumbai–400094, India*
[c] *Department of Chemistry, Pandit Deendayal Energy University, Gandhinagar-382426, Gujarat, India. E-mail: kalisadhanm@yahoo.com*
[d] *Chemistry Division, Bhabha Atomic Research Centre, Trombay, Mumbai-400085, India*

† Electronic supplementary information (ESI) available. See DOI: https://doi.org/10.1039/d4cp04070h

‡ RTP and SP contributed equally to this work.

heterostructures. Mondal *et al.* reported the superior gas sensing property of a ZnO–SnO_2 composite compared with that of pure ZnO nanorods due to the formation of a heterojunction between the grains.[11] Zhao *et al.* synthesized the core–shell-like ZnO–SnO_2 n–n hetero-structured nanowires which exhibit an excellent dual-sensing ability to NO_2 and ethanol.[12] Moon *et al.*[13] fabricated a SnO_2–Zn_2SnO_4 composite-type sensor for CO gas detection. Sun *et al.*[14] reported the improved formaldehyde sensing properties of SnO_2/Zn_2SnO_4. In another study, Zhang *et al.*[15] obtained enhanced trimethylamine gas sensing by fabricating porous Zn_2SnO_4/SnO_2 microspheres and the enhanced sensing behaviour is attributed to the high surface area and formation of a heterojunction between Zn_2SnO_4 and SnO_2. Yang *et al.*[16] fabricated Zn_2SnO_4-doped SnO_2 hollow spheres for sensing phenylamine gas. Due to the porous hollow sphere morphology, the strong interfacial interaction between Zn_2SnO_4 and SnO_2 and the existence of heterojunctions promoted the gas sensing performance.

According to the US Occupational Safety and Health Administration, the maximum permissible exposure limit for *n*-butanol in the workplace is 304 mg m^{-3}. Many other countries also have similar limits.[17] Among all the primary alcohols, *n*-butanol is a colourless transparent organic solvent that has been used as a component in paints, coatings, rubber products, and plastics. However due to its caustic and stimulating nature, *n*-butanol can severely affect the respiratory system, eyes and skin.[17,18] In addition to this, if the air contains a certain concentration of *n*-butanol and the temperature exceeds the flash point of butanol (35 °C), combustion or explosion may occur due to the flammable nature.[19] Moreover, the toxic effects of *n*-butanol are considered, as high as, 6 times that of ethanol,[20] therefore, it is very important to fabricate an efficient, sensitive and selective sensor for the detection of *n*-butanol. There are no reports wherein such composites have been explored for butanol sensing.

Here, in this work, we have designed a composite spinel Zn_2SnO_4 and rutile-structured SnO_2 *via* solid-state reactions. The composite was characterized thoroughly using powder X-ray diffraction (XRD), Fourier-transformed infrared spectroscopy (FTIR), field emission scanning electron microscopy (FESEM), energy dispersive X-ray spectroscopy (EDS) and electron spin resonance (ESR) spectroscopy. The prepared composite capability as a sensor was tested for different gas vapours, *viz.* methanol, ethanol, propanol, butanol, formaldehyde and acetone. The composite exhibits high response, excellent selectivity and good repeatability towards detection of *n*-butanol.

2. Experimental

2.1. Synthesis and instrumentation

The composite Zn_2SnO_4–SnO_2 was prepared using solid-state method. The precursors used for the synthesis, ZnO and SnO_2, were taken in a 1 : 1 molar ratio and ground well and then annealed at 900 °C for 5 h, followed by cooling at room temperature. The powders were again ground well and annealed further at 1200 °C for 5 h. The heating rate for the two steps was 10 °C per min. The final grinding was also carried out for further measurements. The purity of the synthesized composite was checked using a benchtop Proto X-Ray diffractometer with CuKα (1.5405 Å) as the monochromatic X-ray source. FTIR measurement was carried out using a Bruker Alpha FTIR spectrometer in the ATR mode. Morphological study was performed using a field emission scanning electron microscopy (Make: Carl Zeiss, Model: GEMINISEM300). Transmission electron microscopy (TEM), high-resolution TEM (HRTEM), selected area electron diffraction (SAED) and EDS measurements were carried out using Thermofisher, Model: TALOS F200S G2, 200 kV. ESR measurement was performed on a Bruker EMX spectrometer operating in the X-band frequency.

2.2. Sensor fabrication and VOC sensing

Gas sensing measurements were carried out using a static flow system developed in the laboratory. The system was equipped with a sensing chamber, a hotplate coupled with a probe station, a temperature controller, and a source meter (Make: Keithley, Model: 2450). A similar gas-sensing setup has been developed by our research group and was reported elsewhere.[5,7] Thin circular pellets (~1 mm thick and 8 mm diameter) of Zn_2SnO_4–SnO_2 hybrid-composite were prepared from the calcined particles and a parallel Ag strip electrode was deposited on the surface of the pellet. The pellet was used as a chemiresistive sensor element for the sensing studies.

Sensing studies involved different operating temperatures (275–350 °C) of the sensing pellet with varying concentrations of VOCs. Over time, alterations in the surface conductance of the pellet were measured both in the air (C_a) and *n*-butanol vapours (C_g) by applying a voltage to Ag strip electrodes. The sensor response was calculated as C_g/C_a as applicable for the 'n'-type semiconducting Zn_2SnO_4–SnO_2 sensor. The volume (V) of the volatile organic compound in the liquid phase (purity 99.99%), needed to attain the desired vapor concentration in parts per million (ppm) within the closed test chamber, was determined using the following relation (eqn (1))[6]

$$V = \frac{C_g v_c M}{2.46 \times 10^7 \times d} \quad (1)$$

Here, C_g epresents the desired gas concentration in parts per million (ppm), v_c is the volume of the test chamber in millilitres (mL), M denotes the molecular weight of butanol in grams per mole (g mol^{-1}), and d stands for the solvent's density in grams per millilitre (g ml^{-1}).

3. Results and discussion

3.1. Physical characterization

X-ray diffraction was carried out to check the purity of the synthesized material. Rietveld analysis was performed for identifying the phases as shown in Fig. 1(A). It is clear from the figure that the synthesized material is a composite of Zn_2SnO_4 and SnO_2, which matched with the standard patterns of Zn_2SnO_4 (JCPDS no: 24-1470) and SnO_2 (JCPDS no: 41-1445), respectively. The volume

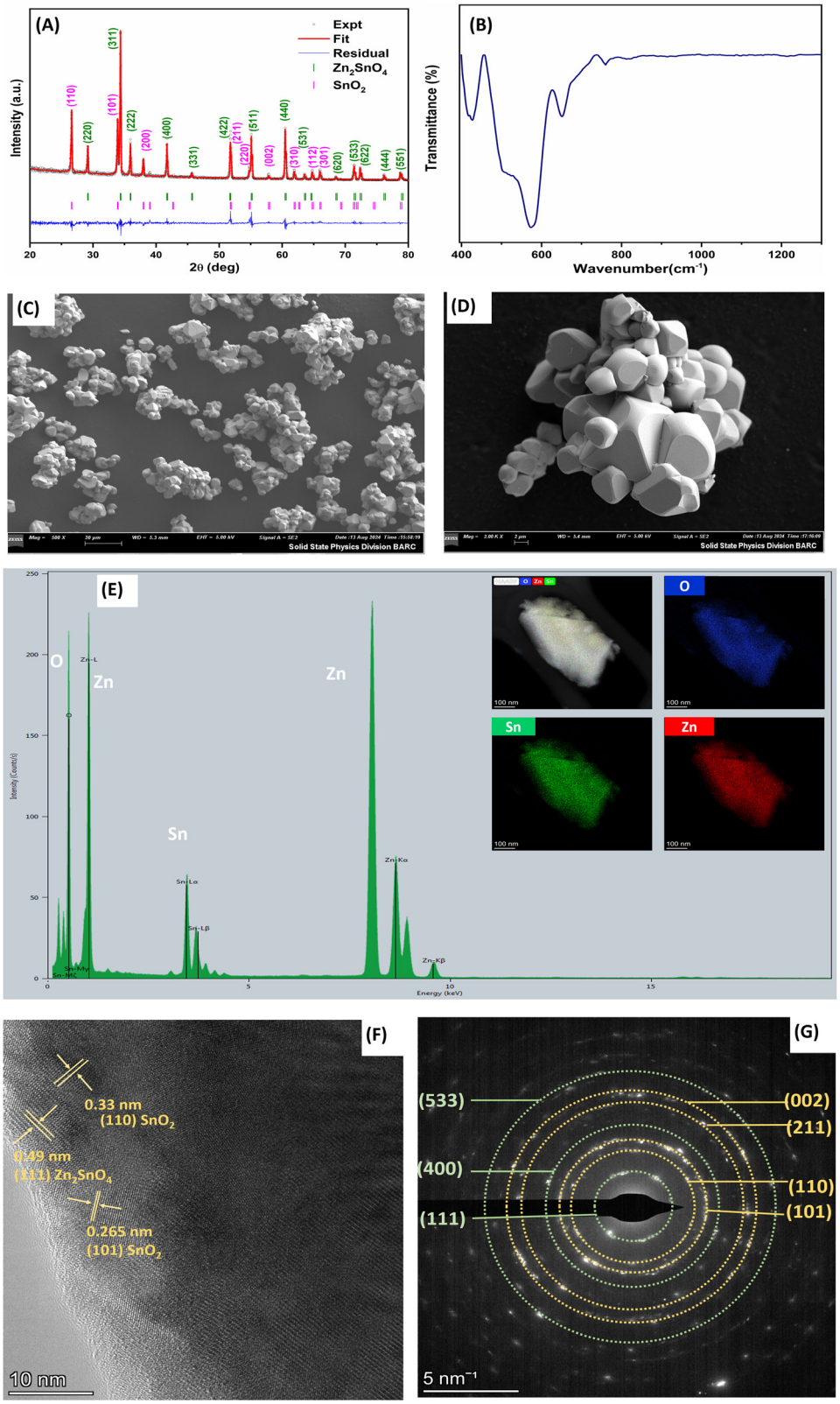

Fig. 1 (A) Rietveld refined XRD patterns, (B) FTIR spectrum, (C) FESEM image, (D) magnified FESEM image, (E) EDS spectrum with inset showing EDS mapping of Zn_2SnO_4–SnO_2, (F) HRTEM image showing lattice fringes corresponding to Zn_2SnO_4 and SnO_2 and corresponding (G) SAED pattern.

fractions of Zn_2SnO_4 and SnO_2 obtained from Rietveld analysis were 72 and 28%, respectively. FTIR measurement was carried out in order to identify the metallic bonds in the synthesized composite, and the data is presented in Fig. 1(B). Here, mainly 3 absorption peaks are observed at 427, 574 and 650 cm^{-1}, which corresponds to M–O bonding (Zn–O or Sn–O), bonding of Zn–O–Sn and vibrations of Sn–O bond, respectively.[5,21,22] Fig. 1(C) and (D) present the FESEM image of the composite under different magnifications. It can be seen from the figure that high-temperature annealing caused the agglomeration of the particles and their size is in the microdomain. However, the image under high magnification showed very clear edges and facets of the composite. The EDS spectrum is shown in Fig. 1(E), which confirms the presence of Zn, Sn and O in the synthesized composite and the inset represents the EDS mapping of the elements, which confirms the uniform distribution of the elements. In cases where composites are synthesized using chemical vapor depositions[23] or atomic layer depositions,[24] it is relatively easier to identify the well-defined interfaces experimentally, as reported previously. However, similar identification of interphases in the case when composites are synthesized using co-precipitation[25] and solid-state methods (current work) is difficult. We could not identify any interface between the SnO_2 and Zn_2SnO_4 phases for both compositions from SEM images.

The structure of the Zn_2SnO_4–SnO_2 composite was further confirmed from the high-resolution TEM studies and selected area electron diffraction (SAED) measurements, as presented in Fig. 1(F) and (G). The d spacing values obtained from the HRTEM image are 0.265 nm, 0.33 nm and 0.49 nm, which correspond to (101), (110) planes of SnO_2[26,27] and (111) planes of Zn_2SnO_4,[28] respectively. From the SAED pattern (Fig. 1(G)) seven diffraction rings correspond to (111), (400) and (533) crystal planes of Zn_2SnO_4 (green circular rings) and (110), (101), (211) and (002) crystal planes of SnO_2, which again confirms the formation of the Zn_2SnO_4–SnO_2 composite.

3.2. ESR and XPS measurements

Fig. 2 presents the ESR spectrum of the Zn_2SnO_4–SnO_2 composite having a resonance signal with a g value of 1.87, which corresponds to Sn defects.[29] To analyse the surface composition and chemical states of the prepared composite, XPS measurements were performed and the corresponding survey scan is shown in Fig. 3(A), which confirms the presence of Zn, Sn and O peaks, which indicates the high chemical purity of the samples. The high-resolution spectrum of Zn 2p is shown in Fig. 3(B) with its two-characteristic peak of binding energy values 1019 eV (Zn $2p_{3/2}$) and 1042 eV (Zn $2p_{1/2}$) with spin–orbit splitting value of 23 eV.[30] This confirms the divalent state of Zn in the composite. The high-resolution spectrum for Sn $3d_{5/2}$ is presented in Fig. 3(C), which is deconvoluted into two peaks having binding energy values of 487.6 eV and 485.4 eV that correspond to Sn^{4+} and Sn^{2+} species.[31] The high-resolution spectrum of O 1s is presented in Fig. 3(D), which can be fitted with 3 peaks of binding energy values. The origin of the peak around 527 eV is not clear, and the peaks at 529.7 eV and 530.7 eV correspond to lattice oxygen and oxygen vacancies.[32] Based on ESR and XPS measurements, it was inferred

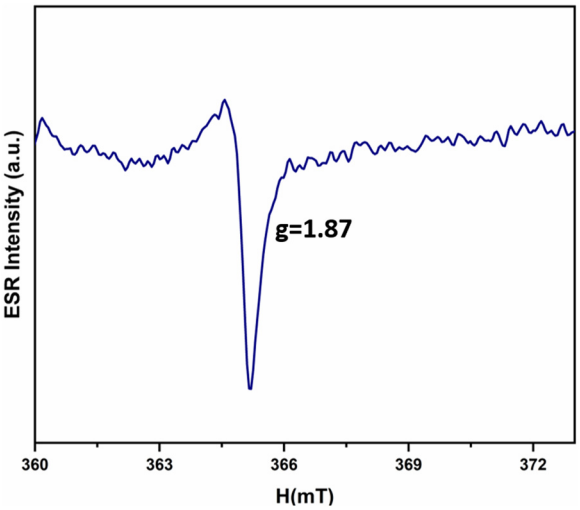

Fig. 2 ESR spectrum of Zn_2SnO_4–SnO_2.

that the Zn_2SnO_4–SnO_2 composite is enriched with both tin and oxygen vacancies that play a profound role in its excellent sensing behaviour towards *n*-butanol.

3.3. *I–V* characteristics of Zn_2SnO_4–SnO_2 composite

The current–voltage (*I–V*) characteristics of the prepared Zn_2SnO_4–SnO_2-based chemiresistive sensor were measured over the voltage range of −20 to 20 V. The sensor showed the linear *I–V* curve passing through the origin at all temperatures, *i.e.* 275, 300, 325, and 350 °C, as demonstrated in Fig. 4(A), which depicts the Ohmic nature of the sensor. The slope of the linear *I–V* curve corresponds to the conductance of the sensor. As the temperature is increased, the conductance of the prepared sensor linearly increases, as illustrated in Fig. 4(B).

3.4. Gas sensing characteristics of Zn_2SnO_4–SnO_2

Fig. 5 shows the schematic of the sensing measurement setup and the chemiresistive sensing mechanism of the prepared Zn_2SnO_4–SnO_2 sensor. The chemiresistive change in the signal due to the sequential interaction of oxygen and reducing vapours (butanol) is explained. As seen from the figure, when the sensor is kept at an elevated temperature, atmospheric oxygen is adsorbed chemically as oxyanions (O_{ad}^-) on the Zn_2SnO_4–SnO_2 surface (eqn (2)) forming an electron-depleted layer, which leads to decreased conductance of the sensor. As shown in eqn (3), the reducing gases (R_g) when exposed to the sensor surface are oxidized by the pre-adsorbed oxygen species (RO_{ad}) resulting in the donation of free electrons to the sensor surface, thus increasing the conductivity of the sensor. During recovery, the RO_{ad} is desorbed from the sensor surface as RO_g upon exposure to air and oxygen is re-chemisorbed, decreasing the conductivity again[33,34] (eqn (4)).

$$O_2 + e^- \leftrightarrow O^-/O^{2-}/O_{2ad}{}^- \quad (2)$$

$$R_g + O_{ad}^- \xrightarrow{k_a} RO_{ad} \quad (3)$$

$$RO_{ad} \xrightarrow{k_d} RO_g \uparrow \quad (4)$$

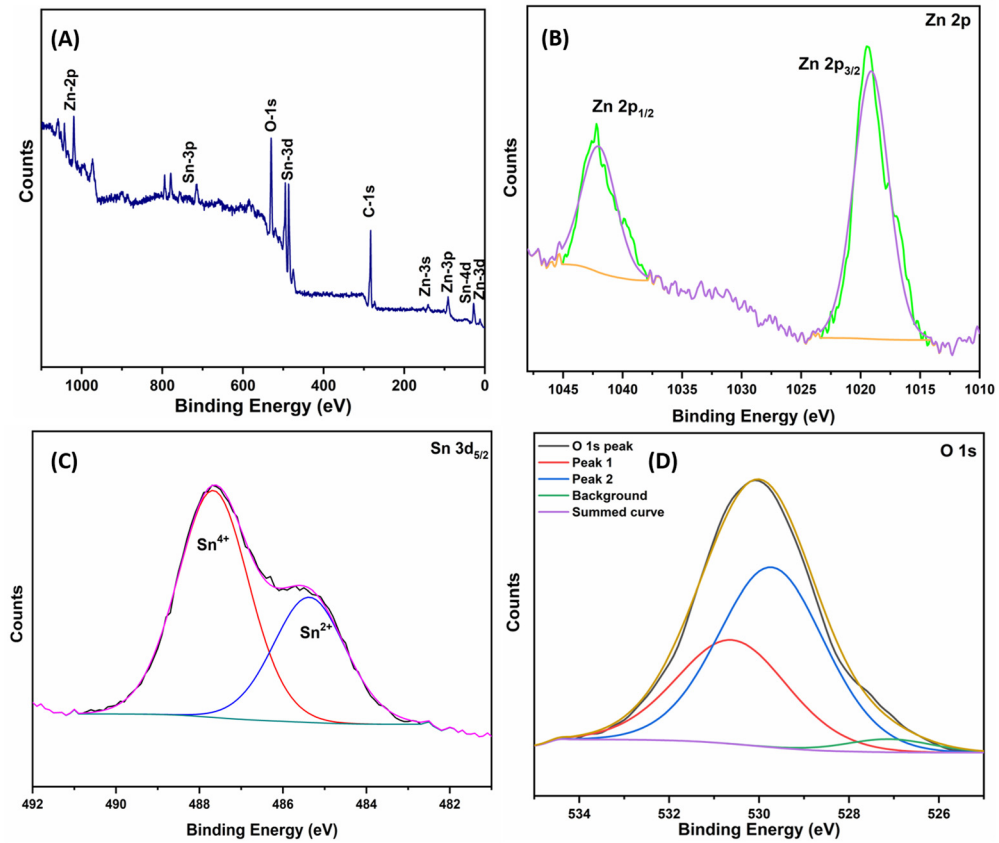

Fig. 3 (A) Survey scan, (B) Zn-2p, (C) Sn-3d and (D) O-1s XPS spectra of the Zn_2SnO_4–SnO_2 composite.

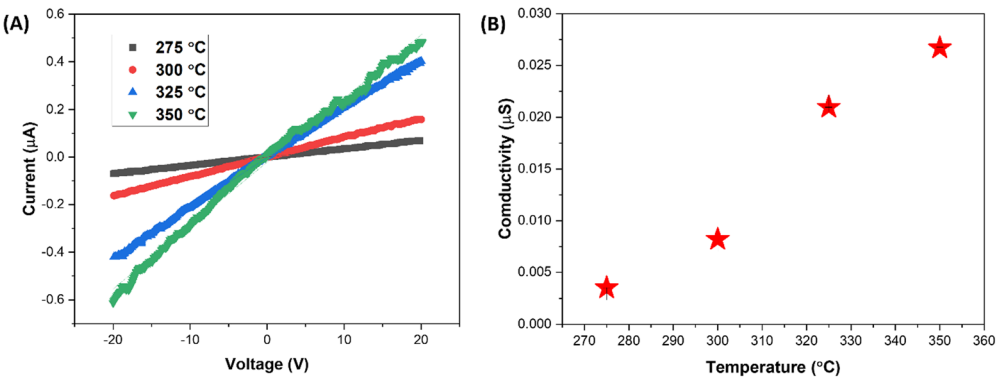

Fig. 4 The *I*–*V* characteristic of the Zn_2SnO_4–SnO_2 composite-based sensor at different temperatures (275–350 °C). (B) The variation in conductance of the sensor with the operating temperature.

In order to assess the cross selectivity of the prepared Zn_2SnO_4–SnO_2 sensor, the sensing study was carried out using 1000 ppm methanol, ethanol, *n*-propanol, *n*-butanol, acetone and formaldehyde consecutively at 300 °C operating temperature (Fig. 6A). The response for each VOC is graphically demonstrated in Fig. 6B. By comparing the response, it seems that the *n*-butanol vapour showed the highest response. In the context of selective sensing of *n*-butanol over other VOCs, principal component analysis (PCA) was employed (shown in Fig. 6C). As envisaged from the figure, PCA enables a clear distinction of patterns for *n*-butanol than the other studied vapors.[35,36]

The variation in the response of the Zn_2SnO_4–SnO_2 sensor when exposed to *n*-butanol at concentrations of 100, 250, 500, and 1000 ppm, sequentially and in reverse (1000, 500, 250, 100 ppm), was investigated at different operating temperatures of 275 °C, 300 °C, 325 °C, and 350 °C, as shown in Fig. 7A–D, respectively. The sensor demonstrated significant repeatability in its response when subjected to the reverse sequence at each temperature, indicating its stability, longevity, and reliability.

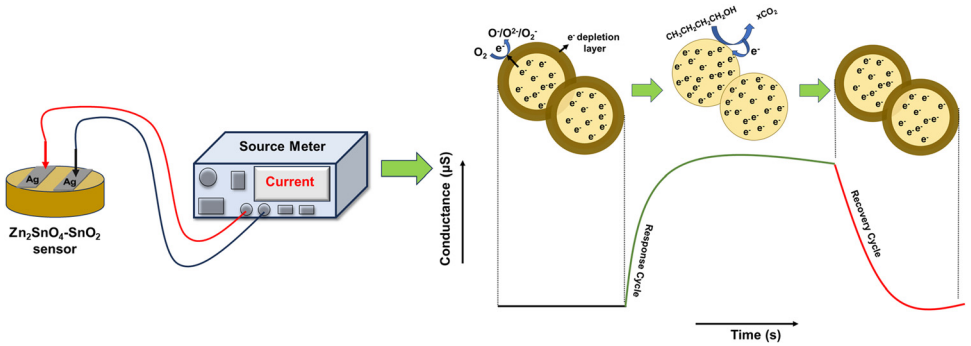

Fig. 5 Schematic of the butanol vapour sensing mechanism using the Zn_2SnO_4–SnO_2 chemiresistor.

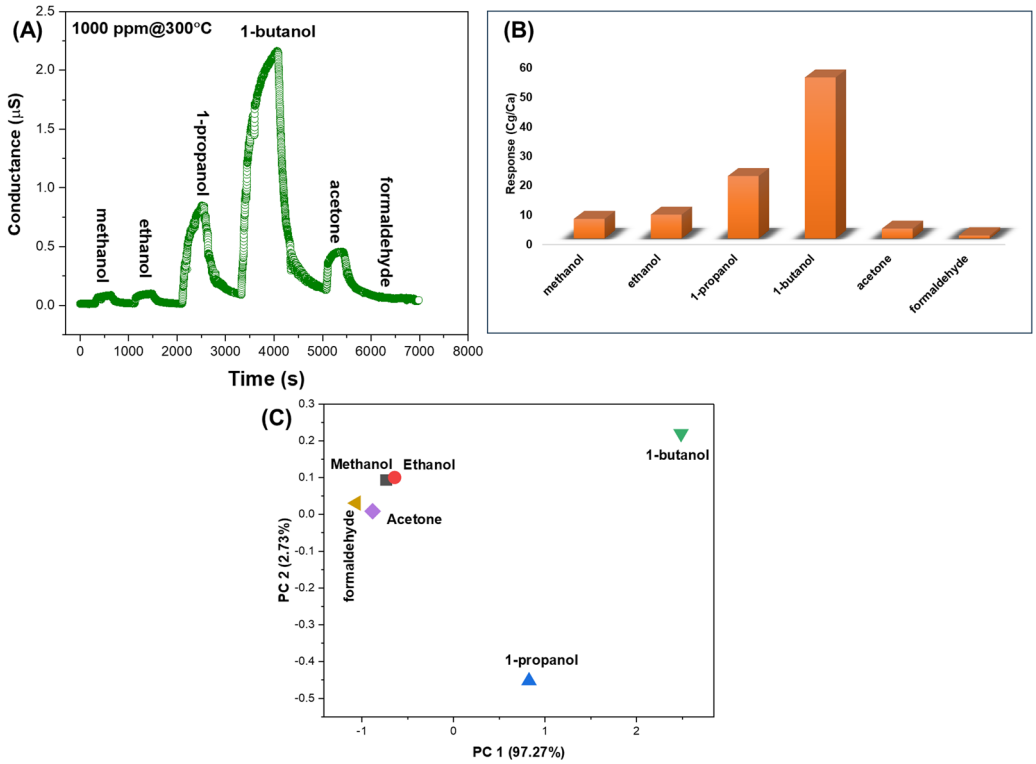

Fig. 6 (A) The conductance transient of the Zn_2SnO_4–SnO_2 composite at 300 °C operating temperature and 1000 ppm concentration for different VOCs; (B) the bar graph representation of the response (C_g/C_a) of different VOCs; (C) PCA for the features of signals acquired for the detection of different VOCs.

The response (C_g/C_a) at each concentration and temperature was calculated and the variation of response with temperature at each concentration (100–1000 ppm) is presented in Fig. 8A. As expected, the response increased with the rising operating temperature for each concentration. This behaviour can be attributed to temperature-dependent oxyanion adsorption on the sensor surface. Higher temperatures facilitate an increased carrier concentration in the conduction band, leading to more extensive oxyanion adsorption and, consequently, an enhanced sensor response. However, optimizing the sensor's operating temperature is crucial, as excessively high temperatures may accelerate the desorption of physisorbed VOC molecules, reducing the sensor's response.

Additionally, the responsivity of the sensor varies with different concentrations of *n*-butanol following the Power law equation proposed by Yamazoe and Shimanoe.[33,37]

$$R = a \times C^n \quad (5)$$

$$\ln(R) = \ln(\alpha) + n\ln(C) \quad (6)$$

where R is the response of the sensor, C is the concentration of the VOC, and α is a constant. 'n' is fairly specific to the kind of target gas and operating temperature, depending on the surface interaction. Fig. 8B shows the linear curve in ln (response) *vs.* ln (concentration) plot following eqn (6), it shows that the linear

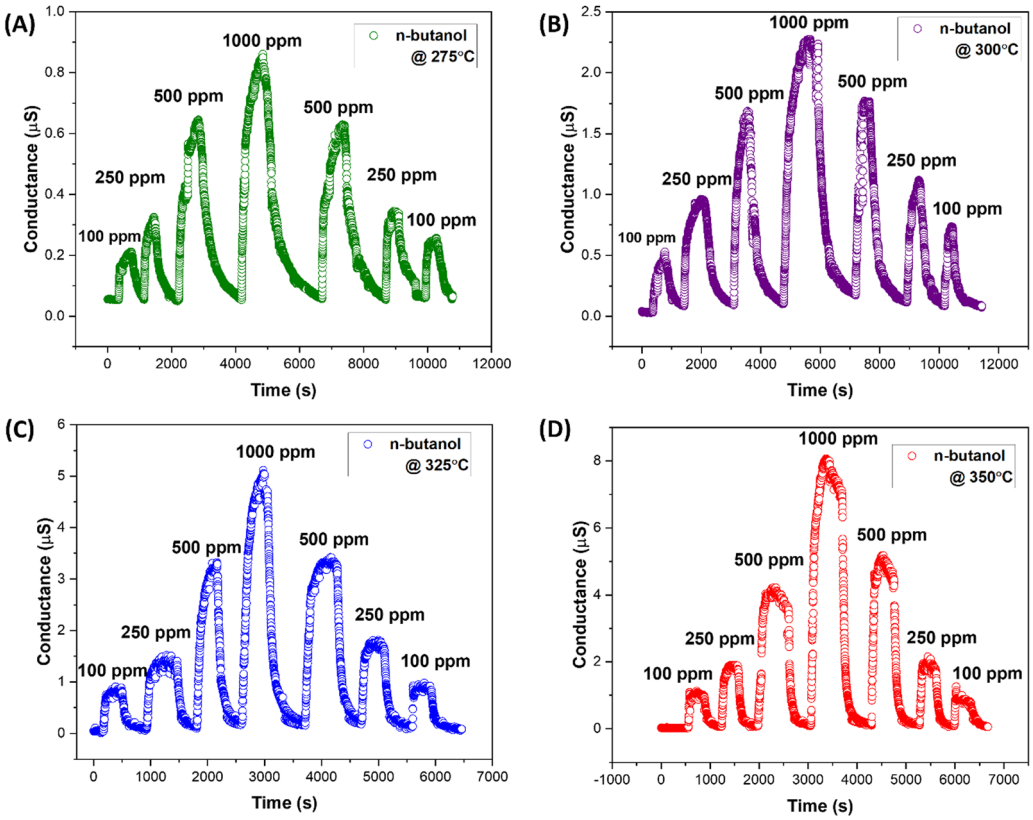

Fig. 7 The conductance transient of the Zn_2SnO_4–SnO_2 composite-based chemiresistive sensor at variable *n*-butanol vapour concentrations (100, 250, 500, and 1000 ppm) at each different temperatures: (A) 275, (B) 300, (C) 325, and (D) 350 °C.

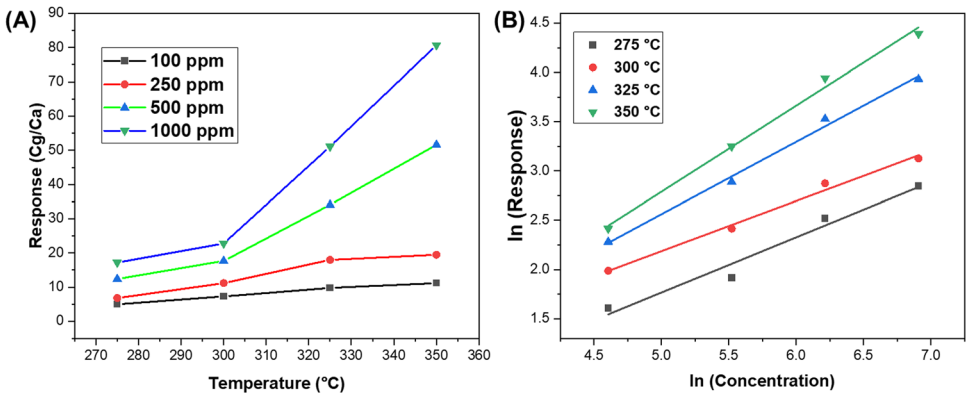

Fig. 8 (A) The variation of response of the Zn_2SnO_4–SnO_2 sensor with temperature change for *n*-butanol sensing at variable concentrations (100, 250, 500 and 1000 ppm). (B) The sensor's response variation with concentration at different operating temperatures (275, 300, 325 and 350 °C).

curves have slope (n) that range between 0.6 and 0.9. It was observed that higher concentrations of *n*-butanol vapor resulted in a stronger response at each temperature, as a greater number of analyte molecules interacted with the oxyanions, leading to an increased return of the carrier electrons to the sensor surface.

The importance of the kinetic analysis is to correlate the experimental data with the established model reaction mechanism for understanding the interactions of the analyte with the sensor surface. As discussed earlier, when the sensor is exposed to butanol, it is oxidised by the pre-adsorbed oxygen species (eqn (3)) forming RO_{ad}. Assuming the monolayer adsorption of butanol on the sensor surface at a constant temperature, T, the conductance transients can be modelled with the Langmuir–Hinshelwood adsorption mechanism. Since the eqn (3) is a rate-limiting step, the rate of the RO_{ad} formation can be written as:

$$\frac{d[RO_{ad}]}{dt} = k_a[R_g][O_{ad}^-] - k_d[RO_{ad}] \quad (7)$$

However, when a gas is introduced or removed, the surface coverage does not instantly reach equilibrium but evolves over time. If it is assumed that at a time, t, the fraction of the surface occupied by chemisorbed oxidised vapours (RO_{ad}) is θ, the remaining unoccupied sites $(1-\theta)$ are filled by the excess oxyanion (O_{ad}^{-}). Given that the concentration of the injected reducing gas, such as acetone and ethanol are C_g, we may write from eqn (7):

$$\frac{d\theta}{dt} = k_a(1-\theta)C_g - k_d\theta \quad (8)$$

where, k_a and k_d represent the adsorption and desorption constants, respectively.

$$k_a = \frac{SN_oK_o}{(2\pi MRT)^{\frac{1}{2}}}\exp\left(-\frac{E_a}{RT}\right) \quad (9)$$

Here, S denotes the surface area of the sensor on which the VOC is adsorbed, K_o is the condensation coefficient, E_a represents the activation energy for adsorption, N_o and R are the Avogadro's number, and universal gas constant, respectively.

The differential eqn (8) can be expressed as assuming the boundary condition that at $t = 0$, $\theta = 0$:

$$\theta(t) = \theta_0\left\{1 - \exp\left[-\frac{t}{\tau_{res}}\right]\right\} \quad (10)$$

In gas sensors, the conductance $G(t)$ of the sensor is typically related to the surface coverage $\theta(t)$ of the adsorbed molecules. Assuming the linear functional dependency between $\theta(t)$ and $G(t)$ and the single adsorption site present on the

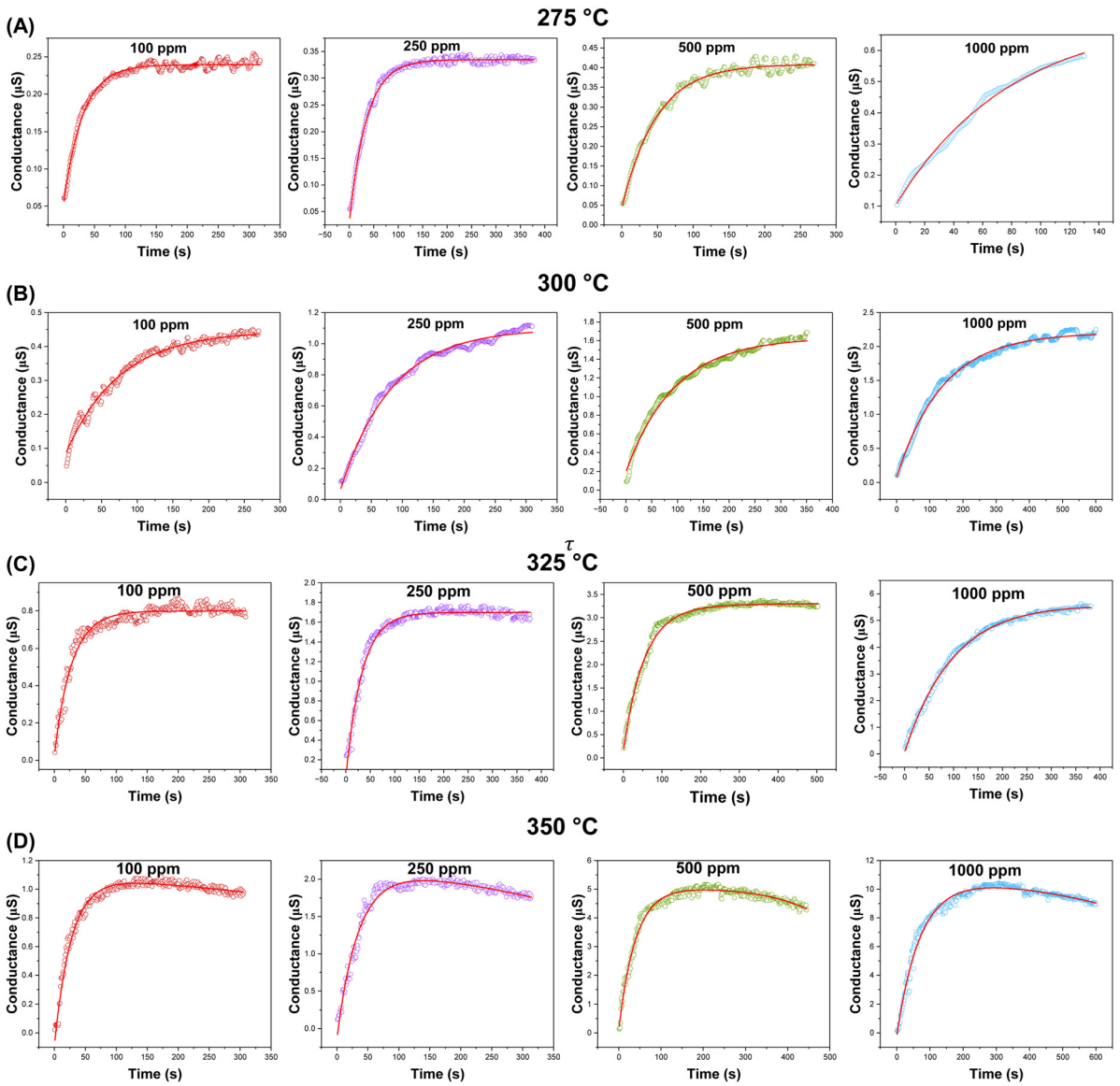

Fig. 9 The conductance transient of the Zn_2SnO_4–SnO_2 sensor in the presence of 100, 250, 500 and 1000 ppm *n*-butanol at different temperatures: (A) 275, (B) 300 °C and (C) 325 °C, (D) 350 °C, fitted using eqn (11) and (12), respectively (red line).

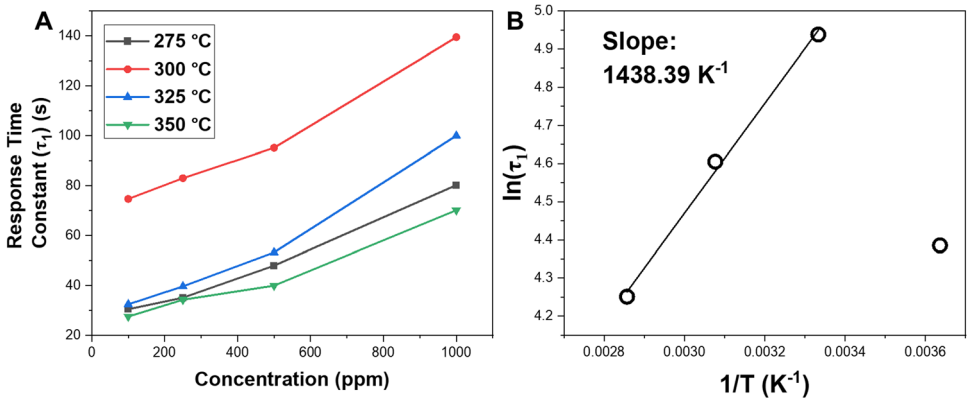

Fig. 10 (A) Response time constant (τ_1) vs concentration plot at various temperature ranges (275–350 °C). (B) The plot of ln (τ_1) *vs.* 1/*T* to determine the activation energy for the oxidation of *n*-butanol.

Zn_2SnO_4–SnO_2 chemiresistor, the conductance variation during response cycle, $G_A(t)$, can be written as:[6,38]

$$G_A(t) = G_0 + G_1\left\{1 - \exp\left[-\frac{t}{\tau_1(\text{res})}\right]\right\} \quad (11)$$

where, G_0 is the baseline conductance of the sensor, G_0 is the change in conductance and $\tau_{1(\text{res})}$ is the response time constant (the detailed derivation is shown in Scheme S1, ESI†).

As presented in Fig. 9(A) and (B), the conductance transient of the Zn_2SnO_4–SnO_2 chemiresistor for four different concentrations (100, 200, 500, and 1000 ppm) each measured at different temperatures (275–350 °C), were fitted with eqn (11). The fitting was good with regression coefficient, $R^2 > 0.98$ for the conductance transients at 275 and 300 °C operating temperature. However, poor fitting was observed for the conductance transient curve at 325 and 350 °C ($R^2 < 0.90$). It can be assumed that at a higher temperature, the oxidation of adsorbed butanol vapour and desorption of the oxidized counterpart simultaneously happened on the sensor surface.[39] Consequently, for higher temperatures, the change conductance (G_t) can be deduced as;

$$G(t) = G_0 + G_1\left\{1 - \exp\left[-\frac{t}{\tau_{1(\text{res})}}\right]\right\} + G_2\left\{\exp\left[-\frac{t}{\tau_{2(\text{res})}}\right]\right\} \quad (12)$$

Here, τ_2 and G_2 represent the characteristic time constant of the desorption step and the change in conductance, respectively. The conductance transients at 325 °C and 350 °C are well-fitted to eqn (12) with an R^2 value of approximately 0.99, as shown in Fig. 9(C) and (D). All fitting parameters for the conductance transients are summarized in Table S1 (ESI†). As inferred from the fitting parameters, the baseline conductance (G_0) remains consistent in the presence of different concentrations of butanol vapor at a constant temperature but increases as the temperature rises. This observation is consistent with the *I*–*V* characteristics mentioned earlier. Fig. 10(A) shows that the response time constant (τ_1) increases with butanol concentration at each operating temperature. At higher concentrations, saturation of the active sensor sites likely slow the adsorption of additional gas molecules, delaying the sensor's equilibrium. The response time constant is inversely proportional to the operating temperature, except at 275 °C, which is attributed to the faster oxidation rate at higher temperatures. The response time constant at 275 °C is noticeably lower than at 300 °C and 325 °C. The response time constant (τ_1) can be expressed by eqn (13),[40]

$$\tau_1 = \tau_0 \exp\left(\frac{E_a}{KT}\right) \quad (13)$$

where E_a and K are the activation energy of the butanol oxidation and Boltzmann constant ($K = 8.6173 \times 10^{-5}$ eV K^{-1}) and τ_0 is a constant. The activation energy can be calculated from the slope of the linearly fitted plot of ln τ_1 *vs.* 1/*T*, as shown in Fig. 10(B). When the SMO sensor is heated at a higher temperature (>300 °C), oxygen is chemisorbed onto the sensor surface predominately as O^-/O^{2-}. In contrast, at lower temperatures, it is primarily adsorbed as O_2^-. Consequently, different oxidation kinetics are likely involved at lower temperatures, leading to an outlier point at 275 °C in the ln (τ_1) *vs.* 1/*T* plot. The estimated

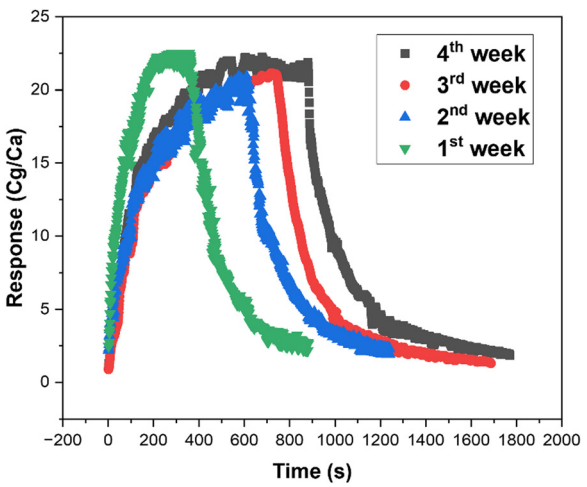

Fig. 11 The response transient of the Zn_2SnO_4–SnO_2 sensor in the presence of 1000 ppm *n*-butanol at 300 °C, monitored at one-week intervals over 4 weeks for stability determination.

Table 1 Comparison of the Zn_2SnO_4–SnO_2 sensor reported in this work with previously reported *n*-butanol sensors

Material	Preparation method	Temperature (°C)	Concentration	Ref.
SnO_2/ZnO	Solvothermal method	200	100 ppm	41
SnO_2/NiO	Electrospinning method	280	100 ppm	42
CdO-decorated ZnO nanobelts	Cation-exchange reaction and calcination	380	20 ppm	43
ZnO–In_2O_3	Co-precipitation hydrothermal method	180	50 ppm	44
In_2O_3-decorated ZnO	Sol–gel method	260	100 ppm	18
Au/SnO_2	Hydrothermal method	80	100 ppm	45
Cd-doped ZnO	Surfactant-mediated method	300	100 ppm	46
Ni-doped ZnO	Co-precipitation and hydrothermal method	300	100 ppm	47
In-doped SnO_2	Hydrothermal co-precipitation method	140	50 ppm	48
$ZnSnO_3$	Mild hydrothermal process	200	50 ppm	49
Zn_2SnO_4	Solid state method	225–300	1000 ppm	5
Zn_2SnO_4–SnO_2	Solid state method	275–350	100 ppm	This work

activation energy of the 1000 ppm butanol oxidation by the pre-chemisorbed oxygen is 0.12 eV.

The long durability and stable response are a crucial characteristic of any sensor. As shown in Fig. 11, the prepared sensor demonstrated a similar response for at least 1 month, which depicted the long-term stability and reliability of the sensor. The sensing performances of the prepared composite were further compared with the previously reported butanol sensors and summarised in Table 1.

Conclusions

To summarise, this work explored the sensing characteristics of the synthesised Zn_2SnO_4–SnO_2 hybrid-composite-based chemiresistive sensor in the presence of *n*-butanol vapours. The detailed characterization study confirmed the formation of the composite, enriched with oxygen vacancies. The cross-sensitivity study of the chemiresistor in the presence of methanol, ethanol, 1-propanol, acetone and formaldehyde demonstrated the enhanced responsivity of *n*-butanol. The sensor exhibited excellent repeatability throughout the temperature range (275–350 °C) in the presence of butanol at four different concentrations (100–1000 ppm). The response magnitude gradually increased with operating temperature, providing the highest response at 350 °C. The conductance transients were kinetically modelled using the Langmuir–Hinshelwood adsorption mechanism. At lower temperatures, the oxidation of *n*-butanol was predominately observed as the rate-determining step, but at higher temperatures the simultaneous oxidation and desorption of oxidized products were prevalent. The estimated activation energy for the oxidation of *n*-butanol by pre-chemisorbed oxyanions was 0.12 eV. Furthermore, the PCA was carried out and the sensor could efficiently discriminate *n*-butanol vapours from other VOCs. Therefore, the present work underscores its importance in discriminating *n*-butanol vapours with the integration of kinetic modelling and statistical approaches. However, the sensitivity measurements of butanol vapour at lower ppm levels, the influence of the humidity in the air, and cross-sensitivity with toxic inorganic gases (H_2, CO, CH_4 *etc.*) can be examined in future studies. Attempts may also be made to develop portable, hand-held miniaturized sensing devices using the prepared materials for real-world application.

Data availability

The data supporting this article have been included as part of the ESI.†

Conflicts of interest

The authors declare no conflict of interest.

Acknowledgements

RTP and SKG would like to acknowledge Dr Vijay Kumar from Centre for Nano and Soft Matter Sciences, Bangalore for HRTEM images and Dr J. Bahadur from Bhabha Atomic Research Centre, Mumbai for FESEM images. The research was funded by the Government of India through the Department of Atomic Energy, India.

References

1 J. Hu, X. Xiong, W. Guan and C. Tan, *ACS Appl. Mater. Interfaces*, 2022, **14**, 55249–55263.
2 Q. Zhang, G. Xie, M. Duan, Y. Liu, Y. Cai, M. Xu, K. Zhao, H. Tai, Y. Jiang and Y. Su, *ACS Appl. Nano Mater.*, 2023, **6**, 17445–17456.
3 Z. Li, H. Yang, L. Zhang, R. Liu and Y. Zhou, *Appl. Surf. Sci.*, 2020, **502**, 144113.
4 X. Yang, Q. Yu, S. Zhang, P. Sun, H. Lu, X. Yan, F. Liu, X. Zhou, X. Liang, Y. Gao and G. Lu, *Sens. Actuators, B*, 2018, **266**, 213–220.
5 R. T. Parayil, B. Bhagat, S. K. Gupta, K. Mukherjee and M. Mohapatra, *Phys. Chem. Chem. Phys.*, 2024, **26**, 7424–7434.
6 B. Bhagat, S. K. Gupta, D. Mandal, R. Bandyopadhyay and K. Mukherjee, *Chem. Phys. Chem.*, 2024, **25**, e202300730.
7 B. Bhagat, S. K. Gupta, D. Mandal, A. A. Gor, R. Bandyopadhyay and K. Mukherjee, *Chem. – Asian J.*, 2024, **19**, e202300841.
8 R. T. Parayil, S. K. Gupta, R. Rohilla, J. Prakash, K. Sudarshan and M. Mohapatra, *ACS Appl. Electron. Mater.*, 2023, **5**, 5151–5163.
9 A. Hermawan, Y. Asakura, M. Inada and S. Yin, *Ceram. Int.*, 2019, **45**, 15435–15444.

10 S. R. Cynthia, R. Sivakumar, C. Sanjeeviraja, C. Gopalakrishnan and K. Jeyadheepan, *Phys. Status Solidi A*, 2020, **217**, 2000512.
11 B. Mondal, J. Das, C. Roychaudhuri, N. Mukharjee and H. Saha, *Eur. Phys. J. Appl. Phys.*, 2016, **73**, 10301.
12 S. Zhao, Y. Shen, P. Zhou, G. Li, F. Hao, C. Han, W. Liu and D. Wei, *Vacuum*, 2020, **181**, 109615.
13 W. J. Moon, J. H. Yu and G. M. Choi, *Sens. Actuators, B*, 2001, **80**, 21–27.
14 G. Sun, G. Ma, Y. Li, Z. Zhang, Z. Chen, Y. Wang, J. Cao and H. Bala, *Mater. Lett.*, 2017, **191**, 145–149.
15 S. Zhang, G. Sun, Y. Li, B. Zhang, Y. Wang and Z. Zhang, *J. Alloys Compd.*, 2019, **785**, 382–390.
16 J. Yang, S. Wang, L. Zhang, R. Dong, Z. Zhu and X. Gao, *Sens. Actuators, B*, 2017, **239**, 857–864.
17 X. Xue, H. Chen, C. Zhang, J. Li, S. Tao, X. Tian, R. Gao, M. Fan, N. Bai and G.-D. Li, *Sens. Actuators, B*, 2024, **419**, 136400.
18 X. Wang, F. Liu, X. Chen, X. Song, G. Xu, Y. Han, J. Tian and H. Cui, *ACS Appl. Nano Mater.*, 2020, **3**, 3295–3304.
19 X. Tian, L. Yao, X. Cui, R. Zhao, X. Xiao and Y. Wang, *Sens. Actuators, B*, 2022, **351**, 130946.
20 Y. Wang, B. Zhang, J. Liu, Q. Yang, X. Cui, Y. Gao, X. Chuai, F. Liu, P. Sun, X. Liang, Y. Sun and G. Lu, *Sens. Actuators, B*, 2016, **236**, 67–76.
21 M. Masjedi-Arani and M. Salavati-Niasari, *J. Mol. Liq.*, 2017, **248**, 197–204.
22 S. S. Niavol, A. B. Khatibani, S. F. Hashemi Karouei, S. A. Hejazi Juybari and H. M. Moghaddam, *Mater. Chem. Phys.*, 2023, **303**, 127799.
23 M. Zhong, Y. Li, I. Yamada and J.-J. Delaunay, *Nanoscale*, 2012, **4**, 1509–1514.
24 M. Nasr, R. Viter, C. Eid, F. Warmont, R. Habchi, P. Miele and M. Bechelany, *RSC Adv.*, 2016, **6**, 103692–103699.
25 M. Baojun, L. Keying, S. Weiguang and L. Wanyi, *Appl. Surf. Sci.*, 2014, **317**, 682–687.
26 J. H. He, T. H. Wu, C. L. Hsin, K. M. Li, L. J. Chen, Y. L. Chueh, L. J. Chou and Z. L. Wang, *Small*, 2006, **2**, 116–120.
27 S. Zhang, G. Sun, Y. Li, B. Zhang, L. Lin, Y. Wang, J. Cao and Z. Zhang, *Sens. Actuators, B*, 2018, **255**, 2936–2943.
28 N. H. Hanh, L. Van Duy, C. M. Hung, N. Van Duy, Y.-W. Heo, N. Van Hieu and N. D. Hoa, *Sens. Actuators, A*, 2020, **302**, 111834.
29 Y. Li, X. Wu, W. Ho, K. Lv, Q. Li, M. Li and S. C. Lee, *Chem. Eng. J.*, 2018, **336**, 200–210.
30 R. T. Parayil, S. K. Gupta, K. Garg, S. Mehta, K. Sudarshan, M. Mohapatra and T. C. Nagaiah, *Sustainable Energy Fuels*, 2024, **8**, 2144–2152.
31 A. d O. Jorgetto, M. V. Boldrin Zanoni and M. O. Orlandi, *Sci. Rep.*, 2023, **13**, 14774.
32 R. T. Parayil, S. K. Gupta, K. Garg, S. Jangra, S. Samanta, K. Sudarshan, M. Mohapatra and T. C. Nagaiah, *Sustainable Energy Fuels*, 2024, **8**, 3136–3144.
33 S. Acharyya, S. Nag, S. Kimbahune, A. Ghose, A. Pal and P. K. Guha, *ACS Sens.*, 2021, **6**, 2218–2224.
34 R. A. B. John and A. R. Kumar, *Inorg. Chem. Commun.*, 2021, **133**, 108893.
35 R. J. Rath, S. Farajikhah, F. Oveissi, F. Dehghani and S. Naficy, *Adv. Eng. Mater.*, 2023, **25**, 2200830.
36 P.-G. Su and M.-C. Li, *Sens. Actuators, A*, 2021, **331**, 112980.
37 N. Yamazoe and K. Shimanoe, *Sens. Actuators, B*, 2008, **128**, 566–573.
38 S. Kulkarni and R. Ghosh, *Appl. Surf. Sci.*, 2024, **665**, 160328.
39 P. Das, B. Mondal and K. Mukherjee, *J. Phys. Chem. C*, 2017, **121**, 1146–1152.
40 T. Bhowmick, S. Nag and S. B. Majumder, *Mater. Chem. Phys.*, 2021, **262**, 124286.
41 Y. Li, L.-X. Shan, R.-C. Wang, X.-X. Lian and Q.-J. Zhou, *Ceram. Int.*, 2022, **48**, 22426–22434.
42 Q. Ma, H. Li, J. Guo, S. Chu, Q. Zhang and Z. Lin, *Mater. Sci. Semicond. Process.*, 2021, **128**, 105762.
43 X.-X. Chen, L. Chen, G. Li, L.-X. Cai, G.-Y. Miao, Z. Guo and F.-L. Meng, *Sens. Actuators, B*, 2021, **334**, 129667.
44 D. An, Q. Wang, X. Tong, X. Lian, Y. Zou and Y. Li, *Ceram. Int.*, 2019, **45**, 6869–6874.
45 S. Wang, J. Guo, Z. Lin, L. Liu, Y. Hui and X. Zhang, *J. Mater. Sci.: Mater. Electron.*, 2022, **33**, 3237–3249.
46 R. Zhao, K. Li, Z. Wang, X. Xing and Y. Wang, *J. Phys. Chem. Solids*, 2018, **112**, 43–49.
47 S. Pan, Y. Guo, G. Chen, L. Sun, J. Huang, L. Wang, L. Cheng and Z. Jiao, *J. Mater. Sci.: Mater. Electron.*, 2022, **33**, 7501–7514.
48 D. An, N. Liu, H. Zhang, Q. Sun, C. Li, Y. Li, Q. Zhang and Y. Lu, *Sens. Actuators, B*, 2021, **340**, 129944.
49 G. Feng, Y. Che, C. Song, J. Xiao, X. Fan, S. Sun, G. Huang and Y. Ma, *Ceram. Int.*, 2021, **47**, 2471–2482.